

The structure of H₂O shells in Mira atmospheres

Correlation with disk brightness distributions and a spectrophotometric signature

A. Tej¹, A. Lançon¹ & M. Scholz²

¹ Observatoire Astronomique de Strasbourg, Université L. Pasteur & CNRS (UMR 7550), Strasbourg, France;
e-mail: surname@astro.u-strasbg.fr

² Institut f. Theoretische Astrophysik der Universität Heidelberg, Tiergartenstr.15, 69121 Heidelberg, Germany,
and School of Physics, University of Sydney, NSW 2006, Australia;
e-mail: scholz@ita.uni-heidelberg.de

Received 19 November 2002 / Accepted 6 January 2003

Abstract. Dynamic models of M-type Mira variables predict the occurrence of water “shells”, i.e. of zones of high H₂O density and high H₂O absorption inside the stellar atmosphere. The density, position and width of these shells is closely correlated with different types of two-component shapes of the intensity distribution on the disk in the *H*, *K* and *L* near-continuum bandpasses. We investigate these correlations and highlight the role of a spectrophotometric H₂O index that warns against serious complications in diameter measurements in the case of substantial water contamination of the bandpass of observation. Simultaneous spectrophotometric and interferometric measurements may allow observers to estimate real continuum diameters more precisely.

Key words. Stars: fundamental parameters – Stars: late-type – Stars: variable: general – Stars: atmospheres

1. Introduction

Studies of Mira variables are of considerable astrophysical interest as these objects are pulsating stars undergoing rapid mass loss and hence play an important role in the enrichment of the interstellar medium. Despite substantial progress in recent years, many fundamental aspects of the physics and structure of Miras still remain unclear. A summary of the present state of knowledge and of crucial problems that have to be solved was given, e.g., in a recent review of Scholz (2002 = S02). Among the most urgent problems is the determination of the stellar diameter that is needed for assigning to the star an effective temperature T_{eff} , for placing the star in the HR diagram, and for understanding pulsation.

Since the pioneer observations of monochromatic radii of *o* Cet and R Leo by Labeyrie and co-workers (Bonneau & Labeyrie 1973; Blazit et al. 1977; Labeyrie et al. 1977; Bonneau et al. 1982) and the first studies of dynamic Mira model atmospheres (Scholz & Takeda 1987; Bessell et al. 1989), it has been known that the atmospheres of M-type Mira variables are geometrically very extended configurations. Layers of formation of strong absorption features may be two or more times as distant from the

star’s centre as the continuum-forming layers. For such an extended-atmosphere star, different diameter definitions may be given (Baschek et al. 1991) and the observed size of the stellar disk depends on wavelength. The most common definition of “the” stellar radius, that describes the global dimensions of the star and is used in modelling the interior and atmospheric structure, is the Rosseland radius R which marks the position of the layer at which the Rosseland optical depth equals unity, $R = r(\tau_{\text{Ross}}=1)$.

Clearly, the Rosseland radius is not an observable quantity, but R is usually close to the continuum optical-depth radius $R_{\text{cont}} = r(\tau_{\text{cont}}=1)$ which depends only slightly on wavelength in the near-IR regime and which in turn may be related via model considerations to an observable intensity radius (e.g. Bessell et al. 1996 = BSW96; Hofmann et al. 1998 = HSW98; Jacob & Scholz 2002 = JS02; S02). Substantial deviations of Rosseland radii from continuum radii are found in very cool M-type Miras in which the Rosseland extinction coefficient is noticeably affected by strong molecular absorption in high layers (e.g. HSW98; JS02; S02). The intensity radius (at continuum wavelengths or in an observer’s filter passband) is defined in terms of the shape of the centre-to-limb variation (CLV). CLV reconstruction from interferometric data is in principle possible but not yet feasible with presently

available accuracies and baseline coverage. In practice, an intensity diameter is derived by fitting observed visibilities with model-predicted visibilities which are characterized by a radius-type parameter. Since molecular layers in the outer atmosphere significantly modify the pure-continuum CLVs, the corresponding visibilities and the resulting diameters, the choice of an appropriate atmospheric model is critical.

Layers of high molecular density may often be considered as a “molecular shell” which is more or less detached from continuum-forming layers depending on the temperature and density stratification of the Mira atmosphere. Indeed, attempts of interpreting near-IR CLVs in terms of H₂O “shells” (e.g. Mennesson et al. 2002a, b) or visual light curves in terms of TiO “shells” (Reid & Goldston 2002) are quite successful. Though this approach is useful and illustrative, one must keep in mind that these H₂O or TiO shells are not circumstellar but are embedded in the stellar atmosphere, and quantitative interpretation of the effects upon CLVs and spectra may only be achieved in terms of molecule densities within the framework of the star’s dynamic model atmosphere (e.g. Bessell et al. 1989; BSW96; HSW98; Höfner et al. 1998; Woitke et al. 1999). Model-predicted, shell-type molecular layers of water and various metal oxides were quoted by Scholz (1992; models of Bessell et al. 1989) and Woitke et al. (1999). ISO and ground-based spectroscopic observations also point to warm layers of H₂O (e.g. Hinkle & Barnes 1979; Tsuji et al. 1997; Yamamura et al. 1999; Matsuura et al. 2002) and other molecules.

In this paper we focus on the characteristics of CLV shapes in the water-contaminated continuum bandpasses in the near-IR. We concentrate our discussion on the *K* bandpass (HSW98; rectangular filter with $\lambda_c = 2.195\mu\text{m}$, $\Delta\lambda = 0.40\mu\text{m}$) as this is the filter which is most commonly used for interferometric observations of Mira variables. We also relate the different classes of CLVs predicted by the models to the time-dependent structure of a pulsating star and to observable spectrophotometric properties. A simple classification is described in Sect. 2. In Section 3, we demonstrate that shells of high water vapour densities are found in the outer layers of most models as a natural consequence of the density and temperature stratification. Their location and extent is shown to relate to the shape of the CLVs, establishing water vapour as an important actor on the scene of angular diameter measurements. In Sect. 4, we show that spectrophotometric indices sensitive to water bands can in principle warn the interferometric observer against the presence of visibility distortions and provide estimated corrections to angular diameter values derived in the uniform disk approximation. However, the reliability of these corrections depends on the precision and the parameter coverage of predicted model spectra for individual observed stars. In a forthcoming paper (Tej et al. 2002 in preparation), we will provide an extensive comparison with empirical optical to near-IR spectra.

2. Classification of CLVs

In this paper we investigate the CLVs predicted by the models of BSW96 and HSW98. For the HSW98 models (P, M, O series), the pulsation is driven by complete self-excited configurations whereas, for the BSW96 models (Z, D, E series), a conventional piston approach to the sub-atmospheric layers is used. The density stratifications result from the shock front driven outflow and the subsequent infall of matter. Non-grey temperature stratifications are computed in the approximation of local thermodynamic and radiative equilibrium. Computationally smeared-out density discontinuities occur at shock front positions. We refer the reader to BSW96 and HSW98 for detailed discussions on the construction of these dynamical models.

The models of Bessell et al. (1989), BSW96 and HSW98 predict a large variety of CLV shapes. These range from nearly uniform and moderately darkened disks to complex CLVs with Gaussian-like or two-component appearance. The model study of JS02 shows that pure-continuum intensity diameters in the near-IR may be accurately defined in terms of the position of the steep flank of the CLV. The resulting visibilities of interferometric observations of the stellar disk may readily be fitted by a moderately darkened disk, and simple uniform-disk (UD) fits lead to reliable continuum diameters with errors of the order of only a few percent. This study also shows, however, that the standard near-IR continuum bandpasses in the 1.2 to 4.0 μm range (*J*, *H*, *K*, *L*) are noticeably contaminated by atmospheric water absorption in Miras with low effective temperatures and strongly extended atmospheres. The CLV has a two-component shape consisting of a moderately darkened inner continuum portion and an outer tail- or protrusion-type extension. The two-component shape of the brightness profile generated in the Rayleigh-Jeans part of the Planck function by modest molecular absorption can well be understood in terms of basic radiation transport (Scholz 2001). The resulting visibility appears distorted as compared to the pure-continuum visibility. Pronounced protrusions may mimic a Gaussian-like shape of the full CLV. The detailed discussion of JS02 shows that these effects lead to serious consequences for measuring continuum diameters. Here, we restrict our investigations and discussions to these two-component CLVs. Figure 1 displays the model CLVs for the *K* passband. The parameter of the non-pulsating “parent” star and the time series of the Mira models are discussed in HSW98 and quantities relevant to our study are listed in Table 1 and Table 2. The CLVs can be broadly classified into three groups based on visual inspection. Note that this is a purely qualitative description; a more quantitative one will be introduced in Sect. 4.

- Tail Type (T): The intensity of this tail is model dependent. The turn-over from the flank to the tail feature is usually located near or below 0.2 in the normalized intensity scale. The angle of turn-over also depends on the model. For instance for P20 the turn-over is sharp

Table 2. Parameters of the time series of the Mira models (adapted from BSW96 & HSW98) and classification of model CLVs. The columns: visual phase ϕ_{vis} ; luminosity L ; Rosseland radius R ; 1.04 near-continuum radius $R_{1.04}$ (JS02); effective temperatures $T_{\text{eff}}(R)$ and $T_{\text{eff}}(R_{1.04})$; classification and remarks. An abbreviated nomenclature (letter defining the series followed by the pulsation phase ($\times 10$)) is adopted for the model names.

Models	ϕ_{vis}	L/L_{\odot}	R/R_p	$R_{1.04}/R_p$	$T_{\text{eff}}(R)$	$T_{\text{eff}}(R_{1.04})$	Type	Remarks
Z10	1+0.0	7650	1.10	1.11	3350	3340	N	Intensity falls steeply to zero
Z15	1+0.5	3860	0.89	0.89	3150	3140	T	Sharp turn-over
Z20	2+0.0	7750	1.11	1.12	3350	3340	N	Intensity falls steeply to zero
Z25	2+0.5	3830	0.89	0.89	3140	3140	T	Sharp turn-over
D10	1+0.0	4490	1.04	1.04	3020	3020	N(?)	Small pedestal
D15	1+0.5	2210	0.91	0.90	2710	2720	T	Smooth turn-over
D20	2+0.0	4560	1.04	1.05	3030	3020	N(?)	Small pedestal as in D10
D25	2+0.5	2170	0.91	0.90	2690	2700	T	Smooth turn-over
E08	0+0.83	4790	1.16	1.07	2330	2440	P	Smooth turn-over
E10	1+0.0	6750	1.09	1.09	2620	2630	T	Smooth turn-over
E11	1+0.1	8780	1.12	1.11	2760	2770	T	Smooth turn-over
E12	1+0.21	7650	1.17	1.15	2610	2640	T	Smooth turn-over
P05	0+0.5	1650	1.20	0.90	2160	2500	P	Bump
P10	1+0.0	5300	1.03	1.04	3130	3120	T	sharp low intensity
P15	1+0.5	1600	1.49	0.85	1930	2560	P	Bump
P20	2+0.0	4960	1.04	1.04	3060	3060	T	sharp with higher intensity compared to P10
P25	2+0.5	1680	1.17	0.91	2200	2500	P	Bump
P30	3+0.0	5840	1.13	1.14	3060	3050	T	sharp low intensity
P35	3+0.5	1760	1.13	0.81	2270	2680	P	Bump
P40	4+0.0	4820	1.17	1.16	2870	2880	T	sharp high intensity
M05	0+0.5	1470	0.93	0.84	2310	2420	P	smooth turn-over
M10	1+0.0	4910	1.19	1.18	2750	2760	P(?)	smooth turn-over
M15	1+0.5	1720	0.88	0.83	2460	2530	P	smooth turn-over
M20	2+0.0	4550	1.23	1.20	2650	2680	P(?)	smooth turn-over
O05	0+0.5	5020	1.12	1.00	2050	2130	P(?)	smooth turn-over
O08	0+0.8	4180	0.93	0.91	2150	2170	P	smooth turn-over
O10	1+0.0	7070	1.05	1.01	2310	2360	P(?)	smooth turn-over

Note: P(?) indicates protrusions with atypical characteristics (see text). N(?) indicates quasi-normal CLVs, that do however display a small pedestal.

Table 1. Properties of the Mira “parent” star series (taken from BSW96 & HSW98). The columns: pulsation mode - fundamental (f) or overtone (o); period P ; parent star mass M ; luminosity L ; Rosseland radius R_p ; effective temperature $T_{\text{eff}} \propto (L/R_p^2)^{1/4}$.

Series	Mode	P (days)	M (M_{\odot})	L (L_{\odot})	R_p (R_{\odot})	T_{eff}
Z	f	334	1.0	6310	236	3370
D	f	330	1.0	3470	236	2900
E	o	328	1.0	6310	366	2700
P	f	332	1.0	3470	241	2860
M	f	332	1.2	3470	260	2750
O	o	320	2.0	5830	503	2250

but for E10 it is comparatively smoother. The extent of the tail can also vary as is seen for P40, where the tail is shorter compared to P20.

- Protrusion Type (P): When the strength of the tail increases it appears as a protrusion of the inner disk. The protrusion appears at a high intensity level. The nature of this feature is also strongly model dependent. It can either be in the form of a ‘bump’ as in P35 or a smoother feature as in M15.
- Normal type (N): These display neither tails nor protrusions and are not two-component CLVs. They could be modelled by moderately darkened disks.

Table 2 lists the class assigned to each K band CLV, following the above definitions. The strength of the second CLV component indicates the amount of water contamination and is strongly wavelength-dependent, but the

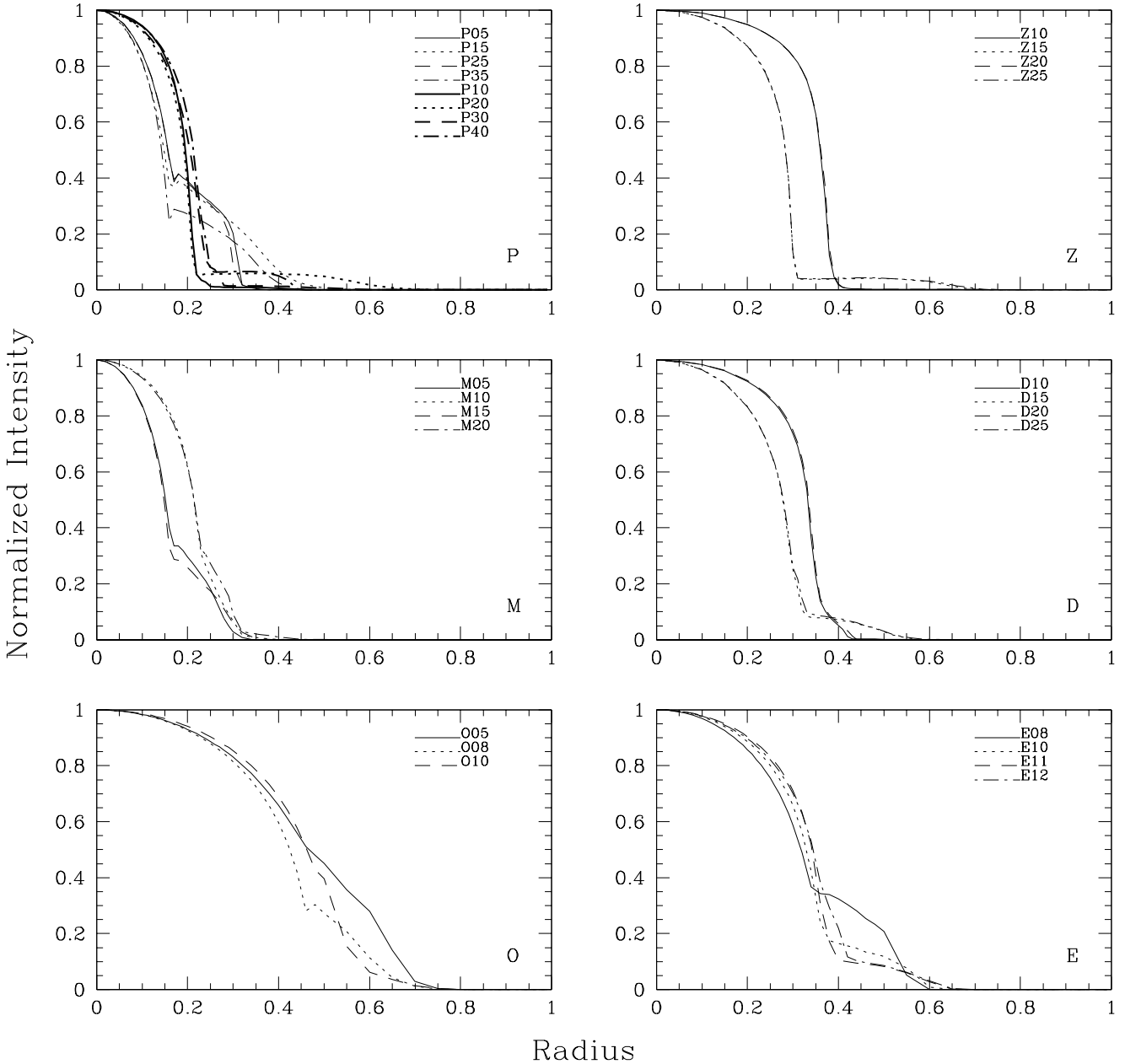


Fig. 1. The model CLVs. The radius is given in arbitrary units (consistent within each panel).

basic characteristics of the brightness profile are the same in the H and L bandpasses with less and more water, respectively, than the K band (JS02). In the near-maximum models of the M series, a protrusion-type attachment to the inner CLV is seen which is inconspicuous and almost merging with the inner CLV, in particular in the H band where water absorption is quite modest. In the very cool first-overtone O models, the H₂O-generated protrusion is strong, but it appears only in the near-minimum model O08 as a clearly separable component whereas it blends with the inner CLV in O05 and O10.

It is evident from the plots and the table that a single parameter, such as the phase, alone does not explain the presence of tails or protrusions. For instance, the near-minimum models of the relatively warm Z and D series have tails whereas the cooler P models have protrusions near-minimum light. Average temperature and pulsation mode also play a significant role. If, for the purpose of ordering the classes, we call protrusions stronger features than tails, there is a clear correlation between the strength of the feature and the phase within individual model series. The strongest features are found near-minimum. Note that for the overtone series, which have larger radii and

lower T_{eff} than fundamental pulsators, models show a global shift of the minimum luminosity to ~ 0.8 (BSW96; HSW98). In the subsequent sections it will become evident that the diversity of the CLV shapes seen is due to a combination of the shock propagation, the shape and extent of the water shells and the density and temperature stratification.

3. Water “shells” and their implication on CLV shapes

Recent interferometric observations of Miras by Mennesson et al. (2002b) show a strong increase in the measured UD diameter between the K' and the L' bands. These authors propose a two-layer scenario with a classical photosphere and a detached and extended (~ 3 stellar radii) gas layer to account for this chromatic variation in size. Similar two-layer models are also invoked by Yamamura et al. (1999) to model the ISO/SWS spectra of *o* Cet and Z Cas. A two-layer “slab” model with plane parallel uniform molecular layers of H₂O placed one above the other is shown to accurately fit the observed spectrum.

We investigate the presence of these water shells in time series of Mira models and their implication on the shape of the CLVs. To display the shells, we use the quantity $\rho \times P_{\text{water}}/P_{\text{gas}}$, where P_{gas} is the total gas pressure and P_{water} the partial pressure of H₂O. It measures the density of water molecules. In Figures 2 and 3, we plot the P models illustrating the protrusions and tails respectively. For Figure 2, we show the P05, P15 and the P35 model CLVs (P25 is essentially identical to P05) and for Figure 3, we plot the P10, P20 and P40 models (P30 is similar to P40 with a slightly broader continuum disk). The upper panels show this shell parameter as a function of the radius, the middle panels plot the respective CLVs and the lower panels show the density structure for these models. Note that the computational smoothing of the shock fronts slightly affects the detailed behaviour of the corresponding areas in all panels. The profile of the water shells clearly plays a role in defining the shape and strengths of the tail/protrusion component of the CLVs.

For the protrusion-type P models, which occur during minima, the effective temperature is low and there is a steep density gradient after the position of the innermost shock front. Shells are formed relatively close to the continuum-forming layers. For the P05 model, there is a narrow “peak-shell” and the density of the water molecules goes down abruptly at the density discontinuity position of the outer shock front. This manifests itself as a sharp cut-off point on the protrusion feature beyond which the intensity is small. Similar behavior is seen for the P35 model where the density of water molecules sharply decreases at the position of the outer shock front. The water shell in this case is much broader and of low density as compared to the P05 model. This is reflected in the CLV shape where the water component of the CLV decreases rather slowly. In the P15 model, there is no outer

shock front, hence, the water shell is much more extended. The above discussion suggests that the extension of these shells depends significantly on the nature of propagation of shocks.

The water shells for the tail-type P models are of different nature. These occur during maxima and for higher effective temperature. Tails correspond to shells with significantly lower water density than protrusion. The shells are detached from the continuum-forming layers and are located in higher atmospheric regions. P10 has an extended but very-low-density shell. P20 has a higher density and there is an abrupt cut-off in the shell coinciding with the position of the outer shock front. The corresponding CLV has a constant tail feature up to the cut-off point. The shell is much more extended for the P40 model and without the occurrence of a outer shock, the CLV shape remains constant out to larger radii before fading to zero.

In Figures 4 and 5 we show similar plots for the high-mass overtone O and fundamental M models (M15 is similar to M05 and hence not plotted). As can be seen from all these plots there are a variety of shapes, strengths and extensions of these water shells which agree quite well with the variety of shapes seen in the CLVs. A point worth mentioning here is the presence of a sharp spike seen in the shells (for e.g. in the P40, O08, M05 models) close to the continuum-forming layers. This is due to the enormous inward increase of ρ while $P_{\text{water}}/P_{\text{gas}}$ is still non-zero. This does not affect the two-component CLVs but results in some additional darkening of the normal continuum disk.

Apart from the very good one-to-one correlation seen between the water shells and the shapes of the CLVs, in general we see that the shells are detached and more extended for the tail-type models as compared to the protrusion-type ones. This is in gross agreement with the results of Yamamura et al. (1999) who surmise that H₂O layers are more extended at maxima. Mennesson et al. (2002b) derive a photospheric radius of 10 mas and a H₂O envelope extending from 15 mas to 27 mas for R Leo. This “gap” of $1.5 R_{\star}$ between the continuum layer and the H₂O envelope is in good agreement with the shells seen for the tail-type P models. Occurrence of such “gaps” is the natural consequence of the temperature-density requirement of the equation of state for H₂O formation.

The density stratification of various molecules exhibits shell-like structures at locations similar to those of H₂O, though with differing relative strengths and extents (cf. Witke et al. 1999). For the models used here, JS02 found that molecular contamination of the H , K and L^* continuum bandpasses is essentially due to H₂O with small contributions of OH and CO in the H bandpass. Hence, molecules other than H₂O probably do not appreciably affect the CLVs and the corresponding visibilities in the near-IR passbands. However, one should be aware that different filter profiles may result in different molecular contributions, that the parameter range and phase-cycle coverage of the models is limited, and that model assumptions and adopted model opacities may play a role. For instance, the BSW96 and HSW98 models used here as-

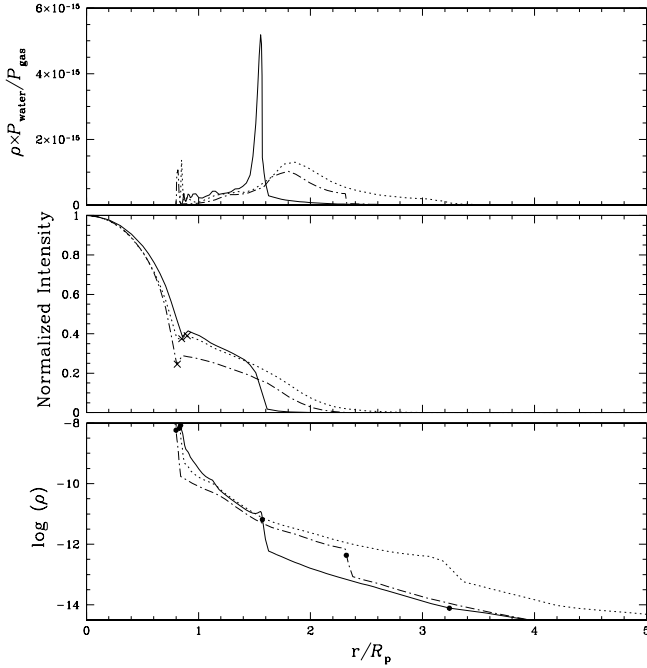


Fig. 2. The relation between the the water “shells” (upper panel), the CLV shapes (middle panel) and the density structure (lower panel) for the near-minimum P model CLVs. The line identifications are P05 - solid; P15 - dotted; P35 - dash-dotted. R_p is the radius of the static parent star (Table 1). In the middle panel the positions of the continuum-forming layer ($R_{1.04}$) are shown with crosses. In the lower panel the location of the shock fronts (computationally smeared out) are marked with filled circles.

sume local thermodynamic equilibrium, whereas Woitke et al. (1999) have shown significant deviations from equilibrium for four molecules including H₂O. Also, variations of metallicities and of C/O ratios (transition to MS- and S-type Miras) are not considered in the present models.

Finally, some interferometric and spectroscopic observations indicate that inner edges of dust shells might be as close as 2 or 3 continuum radii from the star’s centre (e.g. Danchi et al. 1994; Danchi & Bester 1995; Lobel et al. 2000; Lorenz-Martins & Pompeia 2000). M-type Mira models with thermodynamically coupled dust (Bedding et al. 2001) show two-component CLVs similar to those produced by molecular layers for the 1.04 μ m bandpass, a bandpass that is not significantly contaminated by molecules otherwise. The distortions are shown to be pronounced around and below 1 μ m but the effects are almost negligible for the H , K and L^* passbands. The situation is likely to depend strongly on the treatment of dust condensation, and further theoretical work will be useful. For C-type Mira atmospheres, dust condensation is significant in existing models (e.g. Höfner et al. 1998), but these stars lie outside the scope of our paper.

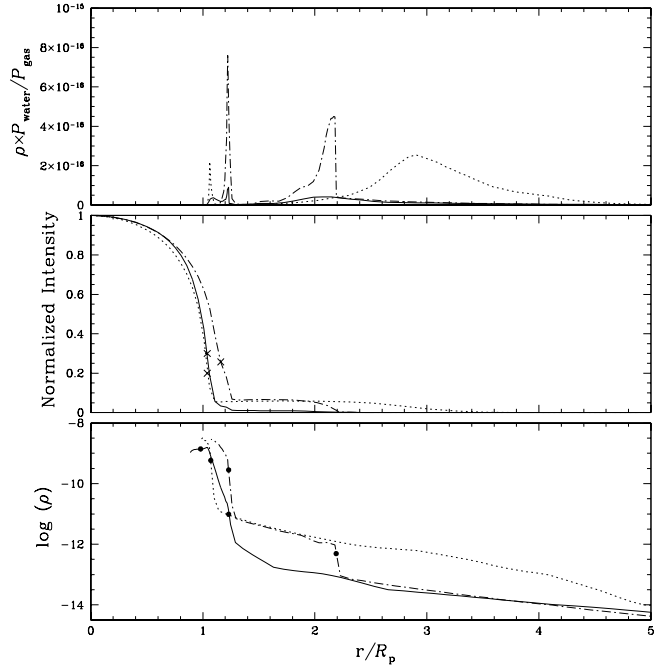


Fig. 3. Same as in Fig. 2 for the near-maximum models P10 (solid), P20 (dotted) and P40 (dash-dotted).

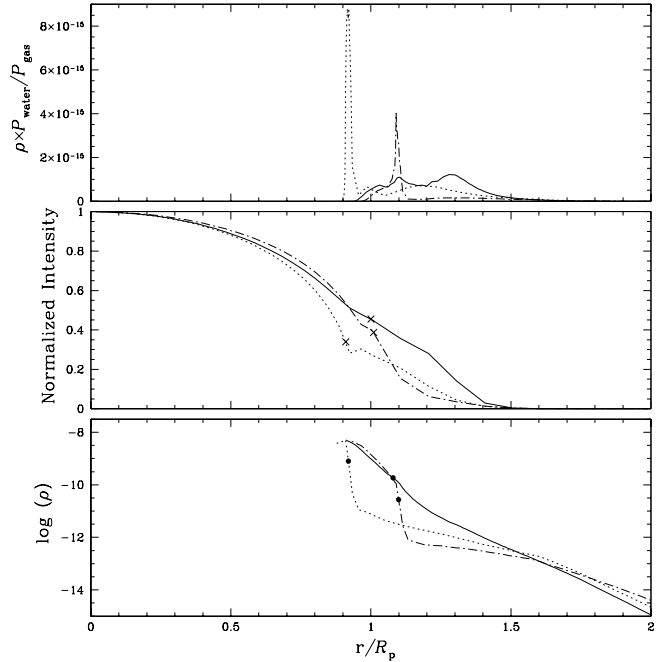


Fig. 4. Same as in Fig. 2 for high-mass overtone models O05 (solid); O08 (dotted) and O10 (dash-dotted).

4. Spectral indications of visibility distortions

In the previous section we have discussed the occurrence of water shells, due to absorption in the outer atmospheric layers, and their effects on the shape of the CLVs. JS02 show that this molecular-band contamination can distort visibility curves and make the measurement of pure-continuum diameters of Miras very difficult. Visibility dis-

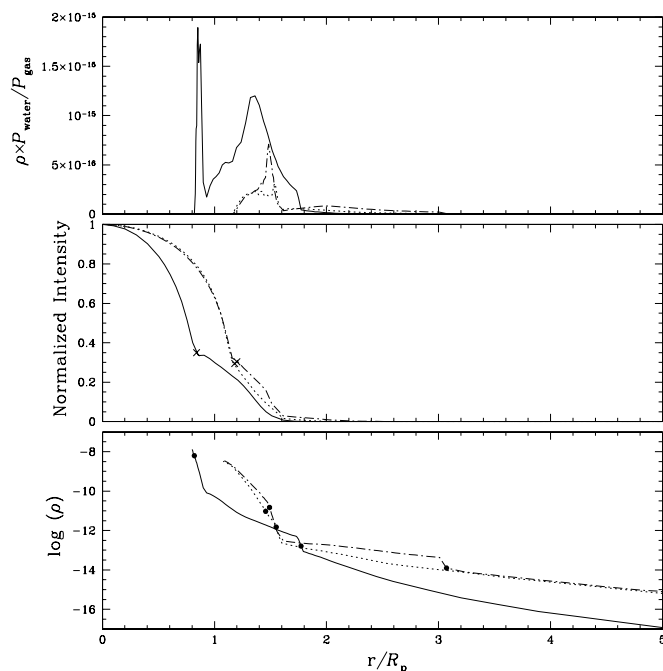


Fig. 5. Same as in Fig. 2 for high-mass fundamental models M05 (solid); M10 (dotted) and M20 (dash-dotted).

tortions are not seen for normal CLVs or those with tiny tail-like features (e.g. P10). In such cases, the diameter estimated by fitting a UD or fully darkened disk to the measured visibilities would represent the near-continuum value. But for models which have tails of high intensity (e.g. P20) the visibilities are highly distorted. The distortions are even more pronounced and are more or less Gaussian in shape for models with protrusion-type CLVs (e.g. P35). Consequently, the fit diameter (by means of a UD or a fully darkened disk) is appreciably dependent on the spatial frequency (i.e. the baseline of observation). Observationally, this effect is seen in the shape of high-precision visibilities with suitable baseline coverage (e.g. Perrin et al. 1999; Weigelt et al. 2002) or in the baseline dependence of UD fit diameters, and in the bandpass-dependence of near-continuum UD fit diameters (e.g. Tuthill et al. 2000; Mennesson et al. 2002b; Thompson et al. 2002; conference reports listed in JS02).

Clearly, the choice of an appropriate atmospheric model and of the corresponding CLV is a critical step in the determination of a stellar diameter. One way of constraining this choice is to combine interferometric observations with many baselines or many wavelengths, and to search a set of atmosphere models for the best fitting ones. With today's instrumentation and relatively poor parameter coverage of the models, this remains cumbersome or impossible. Combining a few interferometric measurements with simultaneous spectroscopy should turn out to be easier. This justifies the search for spectrophotometric indicators of distorted visibilities.

As it now appears, water molecules are the main culprit of the two-component nature of the near-IR CLVs.

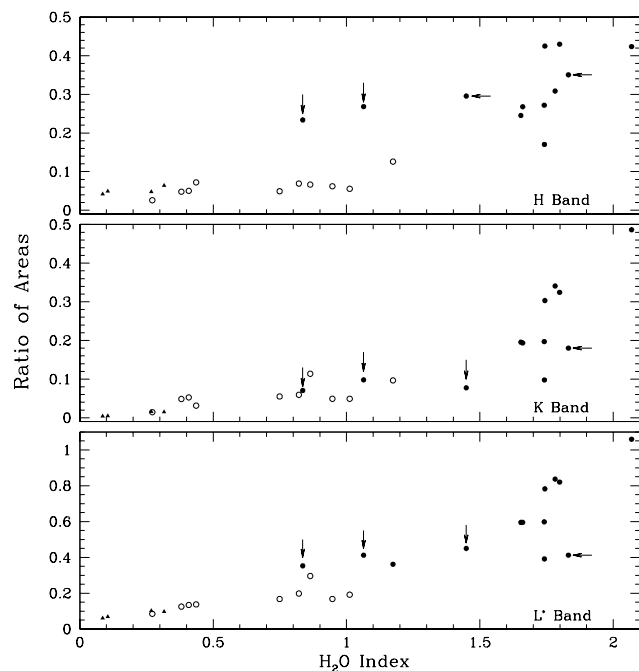


Fig. 6. Strength of the tail/protrusion feature as a function of the H₂O index for the *H*, *K* and *L** bandpasses. The symbols are: filled triangles - normal type CLVs; open circles - tail-type CLVs and filled circles - protrusion-type CLVs. The 4 models with atypical P(?) protrusions in Table 2 (see text) are marked by arrows: M10 (H₂O index 0.84), M20 (1.06), O05 (1.83), O10 (1.45).

Hence, we look for spectrophotometric features which would quantify the amount of water present in Miras. The H₂O index defined by Persson et al. (1977) and Aaronson et al. (1978) is a good indicator, that has been frequently used for classification purposes (Elias et al. 1982; Terndrup et al. 1991; Lançon & Rocca-Volmerange 1992). It measures the ratio of the fluxes measured through narrow-band filters centered, respectively, in the wing of the 1.9 μm water band ($\lambda = 2.0 \mu\text{m}$) and in the *K* band ($\lambda = 2.2 \mu\text{m}$). The index is expressed in magnitudes and is zero for Vega. To quantify the strength of the tail/protrusion feature of the CLVs, we divide the CLV into two parts - the inner disk, and the tail- or protrusion-type extension. The ratio of the area of the extension with respect to the inner disk gives an estimate of the feature strength.

In Figure 6, we show the feature strength as a function of the H₂O index for the *H* band (HSW98; rectangular filter, $\lambda_c = 1.633 \mu\text{m}$, $\Delta\lambda = 0.30 \mu\text{m}$) in the upper panel, the *K* band in the middle panel and the *L** band (HSW98; rectangular filter, $\lambda_c = 3.799 \mu\text{m}$, $\Delta\lambda = 0.60 \mu\text{m}$) in the lower panel. This figure shows the direct correlation between the strength of the CLV extensions and the H₂O index. The strength increases with the increase in the H₂O index. For the *H* and *K* band CLVs the ratio of the areas increases slowly from the normal-types to the tail-types and then there is a steep rise for the protrusion-type exten-

sions. The three large-ordinate points marked by arrows in the upper panel of Figure 6 are atypical P(?) protrusions in Table 2, which are particularly hard to separate in an objective manner from the inner CLV for the *H* band (see Section 2). Water contamination in the near-IR bandpasses is stronger in the *L** band as compared to the *H* and *K* bands (JS02). This manifests in increased strength of the tail/protrusion feature of the CLVs, as clearly seen in the lower panel of Figure 6.

The spectrophotometric index of H₂O gives a satisfactory estimate of the strength of the tail/protrusion feature of the CLV. However, the CLVs are not directly observable quantities but the shapes have a direct implication on the measured visibilities. JS02 have done a detailed study of the effects of phase, cycle and baseline on the measured continuum diameters of different Mira models. They fit UD visibility to the full model-predicted visibilities by means of a least square routine and also carry out single point fits of the UD to the model visibility at three spatial frequencies the choice of which covers the entire range of various model visibilities. The least square fitting to the full model takes care of the arbitrary choice of baselines and the three point fitting gives the baseline dependence of fitted diameters. The near-IR bands show substantial deviation of the fitted UD diameters from the near-continuum values. Apart from uncertainties of model treatment of molecular and dust opacities at very low temperatures, $R_{1.04}$ (the monochromatic radius defined at $\tau_{1.04} = 1$ in the 1.04 μm continuum window) is very close to the continuum value. We refer the reader to JS02 for a detailed discussion of the points outlined above. As an obvious next step, we explore the correlation between the H₂O index and the deviations of fitted UD diameters from the continuum values. We use the *K* band results of Figures 8, 9 & 10 of JS02 for our study.

In the lower panel of Figure 7, we plot the ratio of the least squares fit UD radius (R_{lsq}) to the near-continuum radius ($R_{1.04}$) as a function of the H₂O index. Although the dispersion is large, the deviations of the fitted UD diameters from the continuum values distinctly increases with water contamination. The relation tightens if the overtone models (O and E series) are left out. A linear least squares fit to the model points excluding the overtone models yields

$$R_{\text{lsq}}/R_{1.04} = 0.19 \text{ H}_2\text{O} + 0.89 \quad (1)$$

In the upper panel we plot the correction factor for long baseline observations ($R_{\text{long}}/R_{1.04}$). This baseline is positioned near the first null of the visibility function. It is more sensitive to the details of the CLV structure. The least squares fit to this gives

$$R_{\text{long}}/R_{1.04} = 0.11 \text{ H}_2\text{O} + 0.90 \quad (2)$$

Similar trends are seen for the medium and short baselines (not plotted). The ratios of interferometric UD radii to the Rosseland radius R (instead of $R_{1.04}$) show much more scattered relations to the H₂O index. This is expected because of the nature of the Rosseland opacity which is a

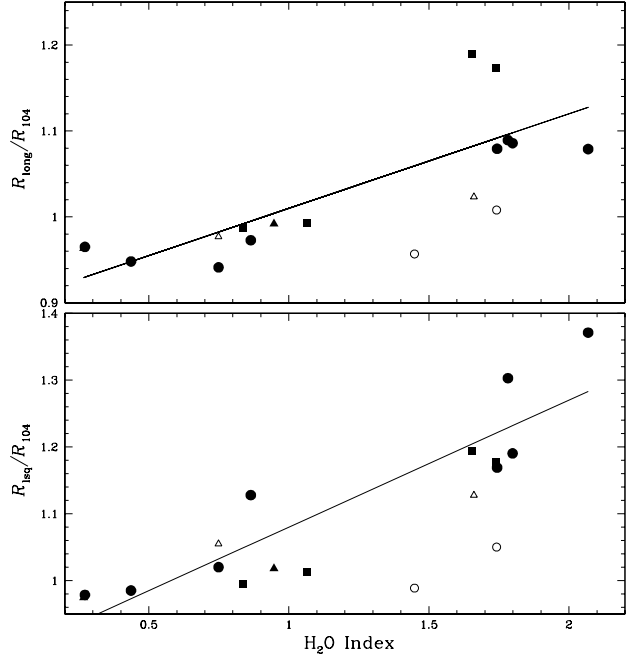


Fig. 7. In this figure we plot the deviations of the UD fitted diameters from the the $R_{1.04}$ for the *K* band. The data points are taken from Figures 8,9 & 10 of JS02. The lower panel shows the results from the least squares and the upper panel shows the long baseline values. The symbols are P models - filled circles; D models - filled triangles; M models - filled squares; O models - open circles; E models - open triangles

harmonic-type mean opacity and is sensitive to extended regions of strong molecular extinction which tends to close the near-continuum windows, to increase the Rosseland opacity and, hence, to increase the Rosseland radius as compared to the continuum radius.

The above two linear fits emphasize the fact that a simultaneous spectral observation of water contamination could yield a correction factor for deriving continuum diameters from the UD fitted values. A couple of caveats should be kept in mind. First, the dispersions in the plots remain large. The situation should improve when more models become available, allowing us to explore the origin of the spreads. For instance, the correlation may depend on other measurable quantities, such as pulsation properties, as suggested by the deviant behaviour of the O series. Second, the exact shape and depth of water bands in spectra is difficult to compute theoretically, in particular in extended, dynamical atmospheres. The reliability of the numerical correction factors given above depends on the accuracy the model spectra and on the range of model parameters explored. As will be shown in a forthcoming paper, current models are successful in reproducing the global features of empirical spectra of Miras and the range of observed water indices, but uncertainties remain large in the time-dependent depths and shapes of individual bands. Once fully satisfactory models exist, other

spectrophotometric measures of the water bands may turn out to be more sensitive to the radius ratios of Fig. 7. The series of BSW96 and HSW98 display a tendency for a broader 1.9 μm band in models with protrusions than in models with tails that remains to be studied in detail.

5. Conclusion

In this paper we have classified the two-component near-IR CLVs predicted by the pulsating Mira models of BSW96 and HSW98 based on a qualitative visual inspection. The models are shown to naturally produce water-rich shells depending on temperature and density stratification of the atmospheric models. The propagation of shock fronts plays a decisive role in the structure and extent of the shells and has direct effect on the shapes of the CLVs. The model-predicted strength of the H₂O index, quantifying the 1.9 μm water feature, gives a good indication of the nature of the CLV in terms of the strength of the tail/protrusion features with respect to the inner continuum disk. The increase in water contamination from the *K* band to the *L* band is evident from the increase in the feature strength for the *L* band CLVs.

Using the results of JS02, we show that the deviations of the fitted UD diameters from the continuum values are correlated with the H₂O index, though with a significant dispersion. The results are based on a moderate number of models covering a limited range of stellar parameters, phases and cycles, which prevents us from identifying the origin of the scatter. The exact form of this correlation still has to be determined from future high-precision visibility observations, and the usefulness of a simple linear approximation as given in Eqs. (1) and (2) still has to be checked both empirically and with more models. Until then, simultaneous spectroscopic observations of water bands may at least warn the interferometric observer and provide a rough estimate of corrections to be applied to the UD fit diameters.

References

- Aaronson M., Persson S. E., Frogel J. A. 1978, ApJ 220, 442
 Baschek B., Scholz M., Wehrse R. 1991, A&A 246, 374
 Bedding T. R., Jacob A. P., Scholz M., Wood P. R. 2001, MNRAS 325, 1487
 Bessell M. S., Brett J. M., Scholz M., Wood P. R. 1989, A&A 213, 209
 Bessell M. S., Scholz M., Wood P. R. 1996, A&A 307, 481 (BSW96)
 Blazit A., Bonneau D., Koechlin L., Labeyrie A. 1977, ApJ 214, L79
 Bonneau D., Foy R., Blazit A., Labeyrie A. 1982, A&A 106, 235
 Bonneau D., Labeyrie A. 1973, ApJ 181, L1
 Danchi W. C., Bester M. 1995, Ap&SS 224, 339
 Danchi W. C., Bester M., Degiacomi C. G., Greenhill L. J., Townes C. H. 1994, AJ 107, 1469
 Elias J. H., Frogel J. A., Matthews K., Neugebauer G. 1982, AJ 87, 1029 (erratum: 87, 1893)
 Hinkle K. H., Barnes T. G. 1979, ApJ 227, 923
 Hofmann K. -H., Scholz M., Wood P. R. 1998, A&A 339, 846 (HSW98)
 Höfner S., Jørgensen U. G., Loidl R., Aringer B. A&A 340, 497
 Jacob A. P., Scholz M. 2002, MNRAS 336, 1377 (JS02)
 Labeyrie A., Koechlin L., Bonneau D., Blazit A. 1977, A&A 218, L75
 Lançon A., Rocca-Volmerange B. 1992, A&AS 96, 593
 Lobel A., Bagnulo S., Doyle J. G., Power C. 2000, MNRAS 317, 391
 Lorenz-Martins S., Pompeia L. 2000, MNRAS 315, 856
 Matsuura M., Yamamura I., Cami J., Onaka T., Murakami H. 2002, A&A 383, 972
 Mennesson B., Creech-Eakman M., Thompson B. B., Perrin G., Coude du Foresto V. et al. 2002a, in: Traub W.A. (ed) Astronomical Telescopes and Instrumentation 2002 - Interferometry for Optical Astronomy II, SPIE Conf. 4838, in press
 Mennesson B., Perrin G., Chagnon G., Coudé du Foresto V., Ridgway S. T., et al. 2002b, ApJ 579, 446
 Perrin G., Coudé du Foresto V., Ridgway S. T., Mennesson B., Ruiler C. et al. 1999, A&A 345, 221
 Persson S. E., Aaronson M., Frogel J. A., 1977, AJ 82, 729
 Reid M. J., Goldston J. E. 2002, ApJ 568, 931 (erratum: 572, 694)
 Scholz M. 1992, A&A 253, 203
 Scholz M. 2001, MNRAS 321, 347
 Scholz M. 2002, in: Traub W.A. (ed) Astronomical Telescopes and Instrumentation 2002 - Interferometry for Optical Astronomy II, SPIE Conf. 4838, in press (S02)
 Scholz M., Takeda Y. 1987, A&A 186, 200 (erratum: 196, 342)
 Terndrup D. M., Frogel J. A., Whitford A. E. 1991, ApJ 378, 742
 Thompson R. R., Creech-Eakman M. J., Akeson R. L. 2002, ApJ 577, 447
 Tsuji T., Ohnaka K., Aoki W., Yamamura I. 1997 A&A 320, L1
 Tuthill P. A., Danchi W. C., Hale D. S., Monnier J. D., Townes C. H. 2000, ApJ 534, 907
 Weigelt G., Beckmann U., Berger J., Blöcker, Brewer M. K. et al. 2002, in: Traub W.A. (ed) Astronomical Telescopes and Instrumentation 2002 - Interferometry for Optical Astronomy II, SPIE Conf. 4838, in press
 Woitke P., Helling Ch., Winters J. M., Jeong K. S. 1999, A&A 348, L17
 Yamamura I., de Jong T., Cami J. 1999, A&A 348, L55